Article

Design and Performance Analysis of Super Highspeed Flywheel Rotor for Electric Vehicle

Pengwei Wang [iD], Tianqi Gu, Binbin Sun *, Ruiyuan Liu, Tiezhu Zhang and Jinshan Yang

School of Transportation and Vehicle Engineering, Shandong University of Technology, Zibo 255000, China
* Correspondence: sunbin_sdut@126.com; Tel.: +86-137-0894-1464

Abstract: The optimal design of a super highspeed flywheel rotor could improve flywheel battery energy density. The improvement of flywheel battery energy density could enhance the performance of the flywheel lithium battery composite energy storage system. However, there are still many problems in the structure, material and flywheel winding of super highspeed flywheels. Therefore, in this paper, electric flywheel energy and power density parameters are designed based on CPE (Continuous Power Energy) function and vehicle dynamics. Then, according to the design index requirements, the structure, size and material of the electric flywheel rotor are designed. Furthermore, the numerical analysis model of stress and displacement of multi-ring interference fit flywheel rotor under plane stress state is established. On this basis, the influence laws of flywheel rotor wheel flange numbers and interlaminar interference on stress distribution of flywheel rotor are analyzed, and the assembly form of wheel flange is determined. Finally, the stress check of the flywheel rotor is completed. The results show that the super highspeed flywheel rotor designed in this paper meets vehicle dynamics requirements in terms of energy storage and power. In terms of strength, it meets the design requirements of static assembly stress and dynamic stress at maximum speed.

Keywords: super high-speed flywheel; rotor design; performance analysis; energy storage system

1. Introduction

The flywheel system studied in this paper is a "mechanical battery" that organically combines a high-speed motor with a high-inertia flywheel. Its charge and discharge process does not involve chemical changes. It has the advantages of green environmental protection, good temperature adaptability, long cycle life and high power density, and it has broad application prospects in electric vehicles [1–3]. Some scholars put forward the concept of a flywheel battery in the 1980s but were limited by the technical conditions at that time, and it has not been widely used. In recent years, with the progress of composite materials, high-speed motors, magnetic bearings and power electronics technology, the research on flywheel batteries has gradually become a hot spot [4].

The development of a highly efficient energy system and the improvement of limited onboard energy utilization efficiency play an important role in extending the mileage range of electric vehicles, a common concern of the electric vehicle industry [5]. At present, using a single lithium battery system as the whole vehicle energy system is the mainstream technology program in the electric vehicle industry. Using a single lithium battery system as the whole vehicle energy system has the advantages of simple topology and lower cost. Still, at the same time, there are problems such as deep coupling between battery working current and vehicle working conditions and low battery working efficiency [6]. Especially driving cycle of the urban, high-load conditions with frequent changes are easy to cause high-current charge and discharge problems of lithium battery, which seriously affects the working efficiency of battery [7,8].

The composite energy storage system scheme based on a super capacitor-lithium battery can effectively improve the working efficiency of a lithium battery by taking

advantage of the instantaneous power intervention advantage of a supercapacitor [9]. However, affected by the lower volume energy density of a super capacitor, the super capacitor-lithium battery composite energy storage system has great installation difficulties in an environment of limited layout space, such as a vehicle, limiting the application of this kind of battery in an electric vehicle, especially in passenger vehicles [10]. The electric flywheel has the same functions and advantages as the supercapacitor and a larger volume energy density, which is conducive to improving the feasibility of its application in electric vehicles [11].

Super high-speed flywheel technology can effectively improve the energy density of flywheel batteries [12]. When the flywheel is running at high speed, the rotor structure and material of the flywheel will have a great impact on its mechanical properties. When the flywheel is running at high speed, the structure and material of the flywheel rotor will have a great impact on its mechanical properties. At present, the research on super highspeed flywheels mainly focuses on the development of highspeed motors, the design and control of magnetic bearing, and the design of the vacuum chamber, while the research on the design and performance of highspeed flywheel rotor is lacking [13,14]. Therefore, in this paper, electric flywheel energy and power density parameters are designed based on vehicle dynamics. Then, the numerical analysis model of stress and displacement of the multi-ring interference fit flywheel rotor is established. Finally, the stress check of the flywheel rotor is completed.

2. Design of Flywheel Rotor Energy and Power Parameters

The flywheel battery mainly comprises a flywheel rotor, flywheel control motor, high-speed bearing, vacuum chamber and DC/DC device, and its basic structure is shown in Figure 1. There are three working modes of flywheel battery: charge, storage and discharge. The specific working principles are as follows, shown in Figure 2.
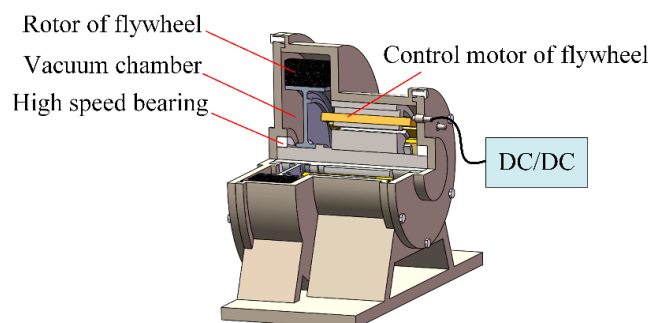

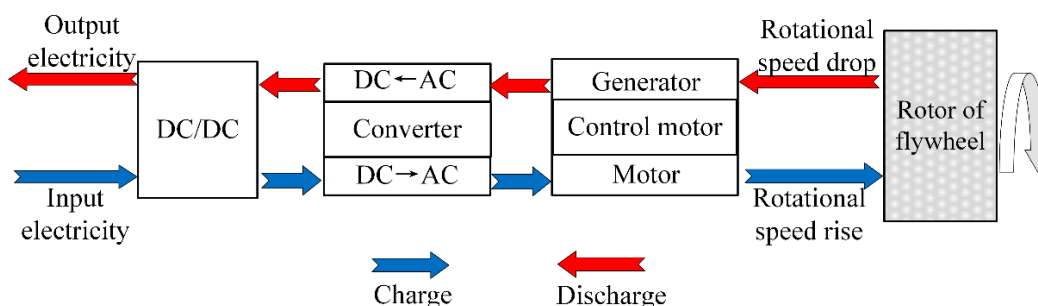**Figure 1.** Schematic diagram of flywheel battery structure.

Figure 2. Flywheel battery energy flow.

(1) Charge mode. The flywheel control motor works in the state of the motor. After the DC/DC device processes the electric energy, the flywheel control motor is driven, and the coaxial flywheel rotor is accelerated. The electric energy is transformed into

the kinetic energy of the flywheel rotation. The flywheel rotor reaches the maximum design speed and can be filled.

(2) Storage mode. The system has neither energy input nor energy output. Due to the use of a vacuum chamber and electromagnetic bearings, the energy loss is very small, and the flywheel is almost maintained at a certain speed.

(3) Discharge mode. The flywheel control motor works in the state of power generation. When the external load has power demand, the high-speed rotating flywheel drives the coaxial flywheel control motor to rotate. The flywheel control motor generates alternating current, and the kinetic energy of the flywheel rotor is converted into electrical energy. The electrical energy is supplied to the load after rectification and transformation. In this process, the flywheel decelerates. The system no longer releases energy when the flywheel speed reaches the minimum design speed.

2.1. Design of Flywheel Rotor Energy Parameters

For an electric vehicle equipped with a flywheel-lithium battery composite energy storage system, the peak power of the whole vehicle, the peak power of lithium battery and the peak power of the flywheel battery shall meet:

$$P_{rep\_max} \leq P_{bat\_max} + P_{fb\_max} \tag{1}$$

where P_{rep_max} is the maximum power required by the vehicle, which can be calculated and determined by the vehicle dynamics equation [15]. P_{bat_max} is the maximum power of the lithium battery, and P_{fb_max} is the maximum power of the flywheel battery.

In order to make full use of the advantage of flywheel instantaneous high power intervention and reduce the power change range of lithium battery, the output power threshold value of lithium battery is set as P_{bat_limit}. When the required power of the whole vehicle is less than P_{bat_limit}, the lithium battery assumes all the required power of the whole vehicle. When the required power of the whole vehicle is greater than P_{bat_limit}, the flywheel battery is used for compensation control.

$$P_{fb} = \begin{cases} 0, & P_{rep} \leq P_{bat\_limit} \\ P_{rep} - P_{bat\_limit}, & P_{rep} > P_{bat\_limit} \end{cases} \tag{2}$$

where P_{fb} is the power of the flywheel battery, and P_{rep} is the required power of the whole vehicle.

The vehicle PE function can be calculated by integrating the power demanded beyond the lithium battery power threshold P_{bat_limit}:

$$F(P_{bat\_limit}) = \begin{cases} 0, & P_{rep} \leq P_{bat\_limit} \\ \int_0^t (P_{rep} - P_{bat\_limit}) dt, & P_{rep} > P_{bat\_limit} \end{cases} \tag{3}$$

Within the continuous working time 0-t of the vehicle, firstly, the driving condition of the whole vehicle can be divided into several periods according to the threshold power P_{bat_limit} of the lithium battery. Further, the PE value in each time period can be calculated according to the PE function. Finally, the maximum PE value in the 0-t time is selected as the CPE value in the whole travel.

$$CPE(P_{bat\_limit}) = \max\{F_i(P_{bat\_limit})\} \tag{4}$$

where $F_i(P_{bat\_limit})$ is the PE value of the ith time period.

According to CPE (Continuous Power Energy) function, the influence of different power thresholds on the coverage ratio of required power under the WLTC (World Light Vehicle Test Cycle) condition is calculated and determined. The power threshold of the lithium battery shall be selected to cover most of the required power of the whole vehicle. If the lithium battery power threshold is too small, the workload of the flywheel battery will

be overloaded. If the lithium battery power threshold is too large, the flywheel battery will not be able to "cut the peak and supplement the valley" of the lithium battery output power. As shown in Figure 3, when the power threshold is 20 kW, the power of lithium battery can cover 78.2 % of the vehicle demand power, and the flywheel battery can also be fully utilized. In summary, the power threshold of the lithium battery in this paper is 20 kW, and the CPE function value is 300 Wh. Considering the flywheel's energy release depth and average working efficiency, the maximum energy storage Efb_max of the flywheel battery can be determined as 370 Wh.
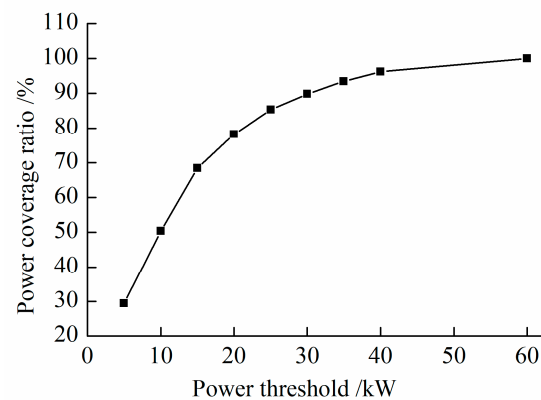
Figure 3. Required power coverage ratio at different power thresholds.

2.2. Design of Flywheel Rotor Power Parameters

The flywheel battery power is calculated according to the difference between the peak demand power of the whole vehicle and the lithium battery power threshold; that is, $P_{\text{fb\_max}}$ should satisfy:

$$P_{\text{fb\_max}} \geq P_{\text{rep\_max}} - P_{\text{bat\_limit}} \tag{5}$$

Under the WLTC working condition, the peak demand power of the whole vehicle $P_{\text{rep\_max}}$ is 59.3 kW, and the lithium battery power threshold $P_{\text{bat\_limit}}$ is 20 kW. Therefore, the maximum power of the flywheel battery $P_{\text{fb\_max}} \geq 39.3$ kW, and take the maximum power of the flywheel battery as 40 kW.

3. Design of Flywheel Rotor Structure and Material

The flywheel rotor is the core energy storage component of the flywheel battery. The maximum energy stored by the flywheel $E_{\text{fb\_max}}$, the moment of inertia j of the flywheel rotor, the maximum working speed of the flywheel ω_{max}, the depth of discharge λ and the minimum working speed ω_{min} satisfy:

$$E_{\text{fb\_max}} = \frac{j\omega_{\text{max}}^2}{2} \tag{6}$$

$$\Gamma = \frac{\omega_{\text{max}}^2 - \omega_{\text{min}}^2}{\omega_{\text{max}}^2} \tag{7}$$

where Γ is the energy release depth of the flywheel.

The moment of inertia of the annular flywheel is:

$$j = \frac{\pi \rho h R_0^4 (1 - \alpha^4)}{2} \tag{8}$$

where h is the height of the flywheel, R_0 is the external diameter of the flywheel, α is the ratio of internal and external diameters, ρ is the material density.

For the flywheel rotor, the energy storage density *e* is an important index to measure its performance, closely related to the maximum velocity speed of the flywheel wheel flange.

$$e = \frac{E_{fb\_max}}{m} = \frac{(1+\alpha^2)v_{Rmax}^2}{4} \tag{9}$$

where v_{Rmax} is the maximum linear velocity of the flywheel rim.

The energy storage density of the flywheel rotor is a direct ratio to the square of the linear velocity of the flywheel rotor wheel flange. The linear velocity of the flywheel rotor wheel flange is restricted by the strength of materials. The limit linear velocity of the common metal materials flywheel rotor wheel flange is generally 300~500 m/s, while the linear velocity of the flywheel rotor wheel flange of high strength composite materials can reach 600~1200 m/s. In order to improve the energy storage density of the flywheel rotor, this paper selects high-strength composite materials to make the flywheel rotor. Owing to the flywheel rotor and the rotation shaft needing precise fit, the machinability of the composite materials is poor, and it is easy to cause delamination damage. Therefore, this paper selects the metal hub to connect the flywheel rotor wheel flange and the rotation shaft. The flywheel rotor structure designed in this paper is shown in Figure 4.
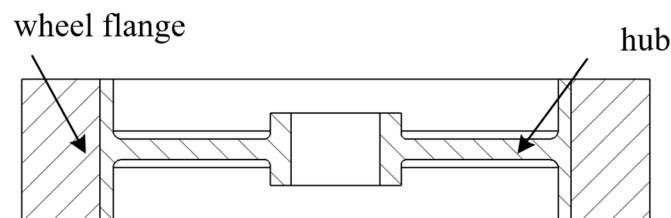

Figure 4. Flywheel rotor structure.

As a new type of fiber material, carbon fiber has the advantages of high strength, high modulus and low density. As a binder, epoxy resin has good adhesion to metals and non-metals and low density. Therefore, epoxy resin is used as the matrix to bond carbon fiber T700 to make the composite wheel flange. The properties of the composite materials are shown in Table 1.

Table 1. Mechanical properties of carbon fiber T700/epoxy resin.

Parameter	Value	Parameter	Value
Circumferential modulus/GPa	150.7	Circumferential shear strength/GPa	5.5
Radial modulus/GPa	7	Radial shear strength/GPa	4.9
Circumferential Poisson's ratio	0.3	Density/kg m^{-3}	1590
Radial Poisson's ratio	0.33	Circumferential strength/MPa	3206

Aluminum alloy materials have the advantages of low density, good plasticity and high strength. Aluminum alloy 7075 is selected as the wheel hub material, and its specific mechanical properties are shown in Table 2.

Table 2. Mechanical properties of aluminum alloy 7075.

Ultimate Strength/MPa	Elastic Modulus/MPa	Density/kg·m^{-3}	Yield Strength/MPa
588	2800	2760	455

After comprehensively considering the material strength, the energy storage density of the flywheel rotor and the laboratory protection conditions, the dimensions of the flywheel rotor are designed according to the flywheel dynamic performance formula and the maximum wheel flange linear velocity v_{Rmax}. The dimensions of the flywheel rotor are shown in Table 3.

Table 3. Geometric parameters of flywheel rotors.

Component	Moment of Inertia/kg m^2	External Diameter/mm	Internal Diameter/mm	Height/mm	Quality/kg
Wheel flange	0.093	300	228	114	5.28
Wheel hub	0.027	228	212	114	2.85

4. Modeling of Flywheel Rotor Stress with Interference Fit

4.1. Modeling Analysis of Single Layer Composite Wheel Flange Stress

When the flywheel rotor rotates around its central axis, it can be simplified as an orthotropic ring of plane stress state only under the action of radial inertial force, and its equilibrium equation is:

$$\frac{d\sigma_r}{dr}+\frac{\sigma_r-\sigma_\theta}{r}+\rho\omega^2r=0 \tag{10}$$

where σ_r is the radial stress, σ_θ is the hoop stress, ρ is the material density, ω is the rotational angular speed, r is the radius.

For anisotropic materials, the relationship between stress and strain is shown in Equation (11).

$$\begin{cases} \sigma_r=\frac{E_\theta}{\lambda^2-v_{\theta r}^2}\left(\varepsilon_r+v_{\theta r}\varepsilon_\theta\right) \\ \sigma_\theta=\frac{E_\theta}{\lambda^2-v_{\theta r}^2}\left(\lambda^2\varepsilon_r+v_{\theta r}\varepsilon_\theta\right) \end{cases} \tag{11}$$

where ε_r is the radial strain, ε_θ is the hoop strain, $\lambda=\sqrt{E_\theta/E_r}$ is the elastic modulus ratio, E_θ is the hoop elastic modulus, E_r is the radial elastic modulus, $v_{\theta r}$ is Poisson's ratio.

The relationship between wheel flange strain and displacement u_r is:

$$\begin{cases} \varepsilon_r=\frac{du_r}{dr} \\ \varepsilon_\theta=\frac{u_r}{r} \end{cases} \tag{12}$$

When the wheel flange boundary is free, the expressions of the radial stress and hoop stress of the flywheel rotor can be obtained as follows [16].

$$\begin{cases} \sigma_\theta=\rho\omega^2r_0^2\frac{3+v_{\theta r}}{9-\lambda^2}[\lambda l(r/r_0)^{\lambda-1}+\lambda(l-1)(r/r_0)^{-\lambda-1}-\frac{\lambda^2+3v_{\theta r}}{3+v_{\theta r}}(r/r_0)^2] \\ \sigma_r=\rho\omega^2r_0^2\frac{3+v_{\theta r}}{9-\lambda^2}[l(r/r_0)^{\lambda-1}-(l-1)(r/r_0)^{-\lambda-1}-(r/r_0)^2] \end{cases} \tag{13}$$

where $l=(\beta^{-\lambda+1}-\beta^2)/(\beta^{-\lambda-1}-\beta^{\lambda-1})$, $\beta=r_i/r_0$ is the ratio of inner radius and outer radius.

4.2. Modeling of Composite Wheel Flange Stress in Multilayer Interference Assembly

Carbon fiber composites are anisotropic materials with high strength along the fiber direction but very low strength perpendicular to the fiber direction. The strength perpendicular to the fiber direction restricts the increase of the flywheel linear velocity. The radial strength of the flywheel can be effectively improved by using a multi-layers interference assembly wheel flange. For the wheel flange of multi-layer interference assembly, it is generally necessary to assemble layer by layer from the inside to the outside, firstly assemble the innermost two layers, then assemble the third layer, and finally to the Nth layer, a total of $N-1$ times of assembly are required. Figure 5 is a schematic diagram of the assembly of a three layers composite wheel flange. After assembly, the first and second layers of the wheel flange are regarded as a whole without initial stress. The inner radius and outer

radius are r_{i1}, R_{o2}, and the inner radius and outer radius ratio is $\beta_2' = r_{i1}/R_{o2}$. Consider the first layer and the second layer as the inner layer and the third layer wheel flange as the outer layer to assemble it.
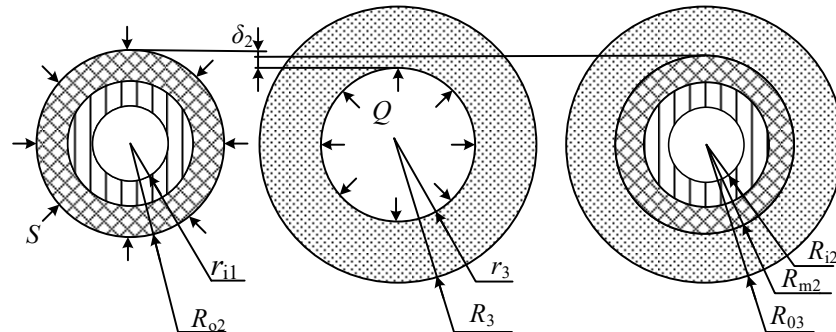

Figure 5. Schematic diagram of three-layer composite rim assembly.

The interference δ_2 is:

$$\delta_2 = R_{o2} - r_3 = R_2 + \frac{2P_1 R_2 \lambda \beta_2^{\lambda+1}}{E_\theta(1-\beta_2^{2\lambda})} - r_3 \tag{14}$$

where P_1 is the pressure at the contact surface of the first layer wheel flange and the second layer wheel flange.

When assembling the third layer wheel flange, the pressure at the contact surface of the second layer wheel flange and the third layer wheel flange is as follows [17].

$$P_2 = \frac{E_\theta \delta_2}{\frac{R_{o2}}{1-\beta_2'^{2\lambda}}[(\lambda-v_{\theta r})+\beta_2'^{2\lambda}(\lambda+v_{\theta r})]+\frac{r_3}{1-\beta_3^{2\lambda}}[\beta_3^{2\lambda}(\lambda-v_{\theta r})+(\lambda+v_{\theta r})]} \tag{15}$$

Under the action of P_2, the radial stress and hoop stress of the inner layer are:

$$\begin{cases} \sigma_r^{2'} = \frac{-P_2}{1-\beta_2'^{2\lambda}}[(r/r_0)^{\lambda-1}-\beta_2'^{2\lambda}(r/r_0)^{-\lambda-1}] \\ \sigma_\theta^{2'} = \frac{-P_2\lambda}{1-\beta_2'^{2\lambda}}[(r/r_0)^{\lambda-1}-\beta_2'^{2\lambda}(r/r_0)^{-\lambda-1}] \end{cases} \tag{16}$$

Under the action of P_2, the radial stress and hoop stress of the outer layer are:

$$\begin{cases} \sigma_r^{31} = \frac{P_2\beta_3^{\lambda+1}}{1-\beta_3^{2\lambda}}[(r/r_0)^{\lambda-1}-(r/r_0)^{-\lambda-1}] \\ \sigma_\theta^{31} = \frac{P_2\lambda\beta_3^{\lambda+1}}{1-\beta_3^{2\lambda}}[(r/r_0)^{\lambda-1}-(r/r_0)^{-\lambda-1}] \end{cases} \tag{17}$$

Then the wheel flange size can be obtained as:

$$\begin{cases} R_{i2} = r_{i1} - \frac{2P_2 R_{o2}\lambda\beta_2'^{\lambda}}{E_\theta(1-\beta_2'^{2\lambda})} \\ R_{m2} = R_{o2} - \frac{P_2 R_{o2}}{E_\theta(1-\beta_2'^{2\lambda})}[(\lambda-v_{\theta r})+\beta_2'^{2\lambda}(\lambda+v_{\theta r})] \\ R_{03} = R_3 + \frac{2P_2 R_3\lambda\beta_3^{\lambda+1}}{E_\theta(1-\beta_3^{2\lambda})} \end{cases} \tag{18}$$

By analogy, the actual interference amount when assembling the Nth layer wheel flange is as follows [17].

$$\delta_{N-1} = R_{0(N-1)} - r_N = R_{N-1} - r_N + \frac{2P_{N-2}R_{N-1}\lambda\beta_{N-1}'^{\lambda+1}}{E_\theta(1-\beta_{N-1}'^{2\lambda})} \tag{19}$$

where $R_{0(N-1)}$ is the outer radius of the wheel flange after $N-1$ times of assembly, β'_{N-1} is the ratio of the inner radius and outer radius of the wheel flange after $N-1$ times of assembly.

When performing $N-1$ assembly, the pressure P_{N-1} of the contact surface is:

$$P_{N-1}=\frac{E_\theta \delta_{N-1}}{\frac{R_{0(N-1)}}{1-\beta'^{2\lambda}_{N-1}}[(\lambda-v_{\theta r})+\beta'^{2\lambda}_{N-1}(\lambda+v_{\theta r})]+\frac{r_N}{1-\beta^{2\lambda}_N}[\beta^{2\lambda}_N(\lambda-v_{\theta r})+(\lambda+v_{\theta r})]} \tag{20}$$

Adding the initial stress of the $N-1$th assembly to the total initial stress of the first $N-2$ assembly, the initial stress of the N-th layer of interference assembly composite wheel flange can be obtained as follows [17].

$$\begin{pmatrix} \sigma_r^1 \\ \sigma_r^2 \\ \sigma_r^3 \\ \vdots \\ \sigma_r^{N-1} \\ \sigma_r^N \end{pmatrix} = \begin{pmatrix} \sigma_r^{11} & 1 & 1 & \cdots & 1 & 1 \\ \sigma_r^{21} & 0 & 1 & \cdots & 1 & 1 \\ \sigma_r^{31} & 0 & 0 & \cdots & 1 & 1 \\ \vdots & \vdots & \vdots & \ddots & \vdots & \vdots \\ \sigma_r^{(N-1)1} & 0 & 0 & \cdots & 0 & 1 \\ \sigma_r^{(N)1} & 0 & 0 & \cdots & 0 & 0 \end{pmatrix}_{N\times(N-1)} \begin{pmatrix} 1 \\ \sigma_r^{1'} \\ \sigma_r^{2'} \\ \vdots \\ \sigma_r^{N-2'} \\ \sigma_r^{N-1'} \end{pmatrix}_{1\times(N-1)} \tag{21}$$

$$\begin{pmatrix} \sigma_\theta^1 \\ \sigma_\theta^2 \\ \sigma_\theta^3 \\ \vdots \\ \sigma_\theta^{N-1} \\ \sigma_\theta^N \end{pmatrix} = \begin{pmatrix} \sigma_\theta^{11} & 1 & 1 & \cdots & 1 & 1 \\ \sigma_\theta^{21} & 0 & 1 & \cdots & 1 & 1 \\ \sigma_\theta^{31} & 0 & 0 & \cdots & 1 & 1 \\ \vdots & \vdots & \vdots & \ddots & \vdots & \vdots \\ \sigma_\theta^{(N-1)1} & 0 & 0 & \cdots & 0 & 1 \\ \sigma_\theta^{(N)1} & 0 & 0 & \cdots & 0 & 0 \end{pmatrix}_{N\times(N-1)} \begin{pmatrix} 1 \\ \sigma_\theta^{1'} \\ \sigma_\theta^{2'} \\ \vdots \\ \sigma_\theta^{N-2'} \\ \sigma_\theta^{N-1'} \end{pmatrix}_{1\times(N-1)} \tag{22}$$

where σ_r^i, $\sigma_\theta^i (i = 1,2,\ldots,N)$ are the initial radial stress and hoop stress of the wheel flange of the i-th layer, $\sigma_r^{i1},\sigma_\theta^{i1}(i = 1,2,\ldots,N)$ is the initial radial stress and hoop stress of the i-th layer wheel flange when assembled to the i-th layer rim, $\sigma_\theta^{i'}$, $\sigma_r^{i'} (i = 1,2,\ldots,N-1)$ is the radial and hoop stress of the inner layer $I-1$ wheel flange when assembled to the wheel flange of the i-th layer.

After the N-layers of the wheel flange are assembled, the inner radius and outer radius dimensions of the overall wheel flange are:

$$\begin{cases} R_{i(N-1)}=r_1-\sum_{i=1}^{N-1}\frac{2P_iR_{0i}\lambda\beta'^{2\lambda}_j}{E_\theta(1-\beta'^{2\lambda}_i)} \\ R_{0N}=R_N+\frac{2P_{N-1}R_N\lambda\beta^{\lambda+1}_N}{E_\theta(1-\beta^{2\lambda}_N)} \end{cases} \tag{23}$$

*4.3. Flywheel Rotor Stress Analysis*

4.3.1. Analysis of Factors Influencing Stress of Flywheel Rotor

(1) Analysis of the influence of the number of wheel flange layers on the stress of the flywheel rotor

Single layer, double layer and three layers wheel flange layers are selected for analysis by commercial simulation software Ansys. The thickness of each layer of wheel flange under the same scheme is the same. Scheme I, II and III correspond to the layer thickness of 36 mm, 18 mm and 12 mm, respectively. The interference between all contact surfaces is set to 0.5 mm. The three-dimensional models corresponding to the three schemes are shown in Figure 6.
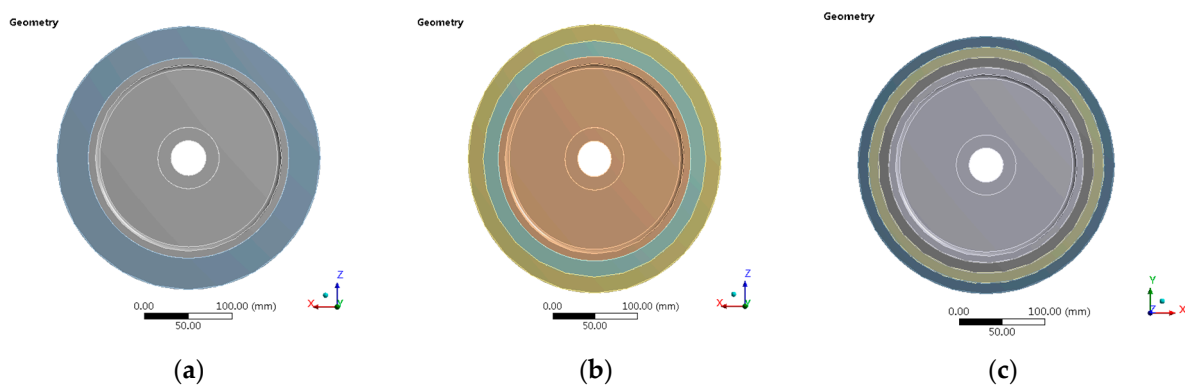
Figure 6. Three-dimensional model of flywheel rotor under different schemes. (**a**) Scheme I; (**b**) scheme II; (**c**) scheme III.

Because there are spokes in the middle of the wheel hub axis, when the flywheel rotor rotates at high speed, the radial displacement at both ends of the wheel hub under the action of centrifugal force must be greater than the middle of the wheel hub. Hence, the middle of the wheel hub is most likely to be disengaged, resulting in the failure of the flywheel rotor. Select the wheel hub tangent as the analysis path. The obtained stress distribution curve is shown in Figure 7. It can be seen that the radial compressive stress on the flywheel rotor is proportional to the number of flange layers under the condition of the same interlayer interference, and the radial compressive stress on the wheel hub increases most obviously with the increase of the number of flange layers. For the circumferential stress, with the increase of the number of wheel flange layers, the maximum circumferential stress on the wheel flange will increase significantly, and a sudden change will occur at the junction of the two layers, showing a step jump increase and gradual decrease from inside to outside in the layer. The radial compressive stress can be generated in the flywheel rotor by using the interference assembly method to improve the radial strength of the flywheel rotor. Still, the increase of the radial strength will sacrifice some of the circumferential strength.
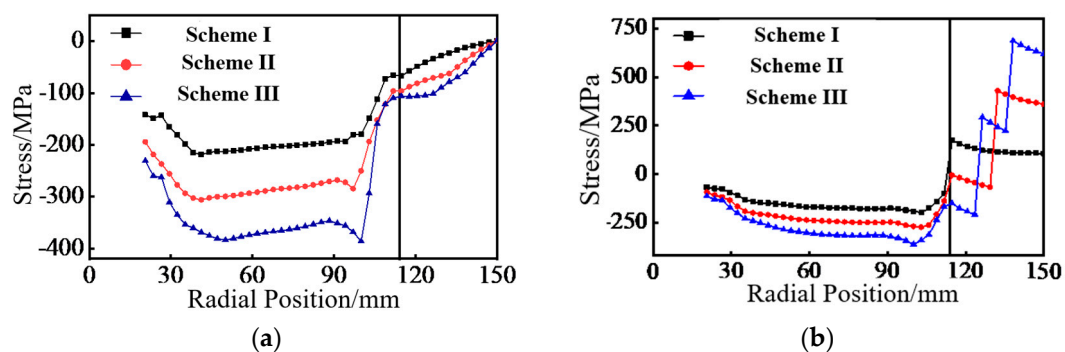
Figure 7. Stress curve of the flywheel at rest. (**a**) Radial stress curve; (**b**) Hoop stress curve.

The stress distribution curve of the flywheel rotor under the maximum speed of each scheme is shown in Figure 8. Due to the centrifugal force, most of the radial compressive stress on the wheel hub is converted into tensile stress. The maximum tensile stress is inversely proportional to the number of the wheel flange layers, and the compressive stress on the wheel flange is also significantly reduced compared to when the flywheel is stationary. In scheme I, the radial stress at the junction of the wheel flange and the wheel hub is 3.77 Mpa, indicating that the interference assembly pressure between the wheel flange and the wheel hub has been completely released, and the flywheel rotor has failed. However, there is still radial compressive stress between the layers of the flywheel rotor in scheme II and scheme III, which can meet the use requirements. The changing trend of hoop stress is similar to that in the static state, but the stress value increases greatly.
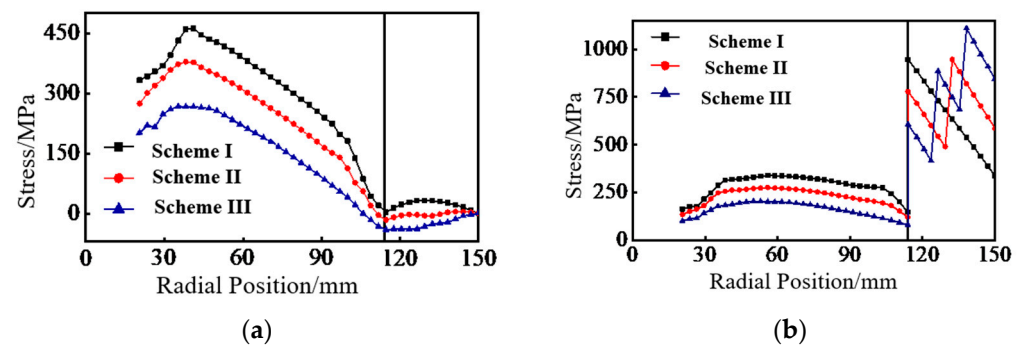
Figure 8. Stress curve of the flywheel at maximum speed. (**a**) Radial stress curve; (**b**) hoop stress curve.

The flywheel rotor assembled with single ring wheel flange interference cannot meet the use requirements when the interference is 0.5 mm. Theoretically, increasing the interference will further improve the strength of the flywheel rotor, but it is difficult to assemble when the interference exceeds 0.5 mm. Multi-layer interference assembly can improve the flywheel rotor's stress level, improve the flywheel rotor's strength, and reduce the machining difficulty of the flywheel rotor. However, the wheel flange cannot be infinitely layered. When there are too many layers, material failure occurs due to excessive radial compressive stress. In this paper, three layers interference assembly scheme III is selected as the structural design scheme.

(2) Influence of Interlayer Interference on Stress of Flywheel Rotor

In order to study the influence of interlayer interference on flywheel rotor stress, the flywheel rotor assembled with three layers of interference is taken as the research object, and the influence of interlayer interference loading on flywheel rotor stress is analyzed under the same overall interference. The setting of interlayer interference under different schemes is shown in Table 4.

**Table 4.** Interference between contact layers.

Scheme	Scheme I	Scheme II	Scheme III
Interference between the inner layer and the wheel hub/mm	0.3	0.4	0.5
Interference between the middle layer and the inner layer/mm	0.4	0.4	0.4
Interference between the outer layer and the middle layer/mm	0.5	0.4	0.3

The stress distribution curve of the flywheel rotor under the static state of each scheme is shown in Figure 9. The maximum radial compressive stress under the three schemes occurs at the contact surface between the inner layer of the wheel flange and the wheel hub. The maximum radial compressive stress on the wheel hub is greatly affected by the interference between the inner wheel flange and the wheel hub. The radial compressive stress on the wheel hub increases significantly with the increase of the interference. The radial compressive stress on the wheel flange has poor transmissibility between the rims of each layer and can only affect the adjacent rims. The hoop stress will jump at the junction of the two layers, and the jump amplitude is proportional to the interference at the junction. The interference between the outer layer and the middle layer will have a great impact on the peak hoop stress. Since the interference at the junction of the wheel hub and inner rim will significantly affect the radial stress on the wheel hub. Therefore, it is necessary to decrease the interference at the junction to avoid fatigue failure caused by the long-term stress of the wheel hub.
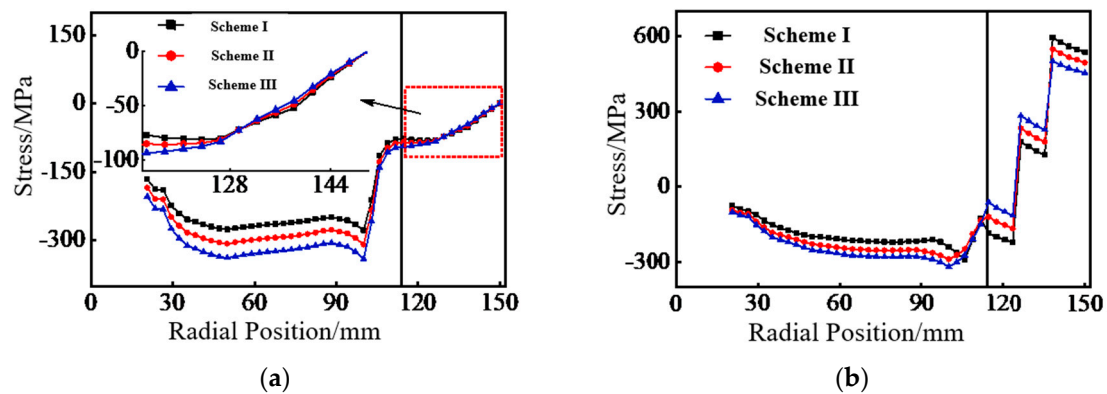
Figure 9. Stress curve of the flywheel at rest. (**a**) Radial stress curve; (**b**) hoop stress curve.

The stress curve of the flywheel rotor at the highest speed is shown in Figure 10. The wheel hub's radial compressive stress has been transformed into tensile stress. The stress value is inversely proportional to the interference between the inner layer of the wheel hub and the rim. The maximum compressive stress on the wheel flange occurs in the inner layer, and the maximum tensile stress occurs in the outer layer of the wheel flange. When a small interference is used between the inner layer of the wheel flange and the wheel hub, and a large interference is used between the outer layer and the middle layer, the overall radial stress level on the wheel flange is low, and the radial stress level in each layer is basically the same, which can effectively prevent fatigue damage of a layer in advance due to high-stress level. In terms of hoop stress, when a small amount of interference is used between the outer layer and the middle layer, the hoop stress level on the whole flywheel wheel flange is low.
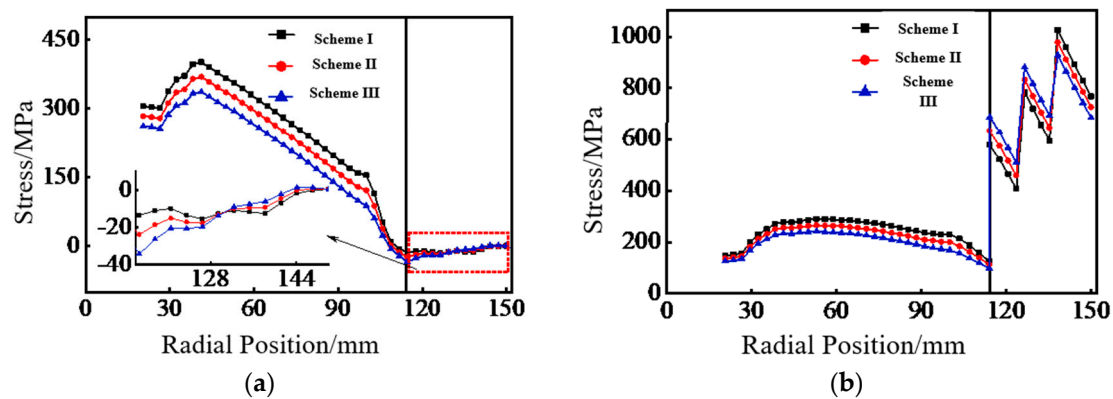
Figure 10. Stress curve of the flywheel at maximum speed. (**a**) Radial stress curve; (**b**) hoop stress curve.

To sum up, from the perspective of improving the stress level of the flywheel rotor, when selecting the interference between flange layers of the flywheel rotor, the smaller interference should be selected in the inner layer of the flange, and the larger interference should be selected in the outer layer. Scheme I is selected as the final design scheme in this paper.

4.3.2. Flywheel Rotor Stress Check

Through the analysis in the previous section, the number of layers of flywheel rotor flange and the interference between layers is determined. This section checks the stress of the designed flywheel rotor to ensure its safety in the working process.

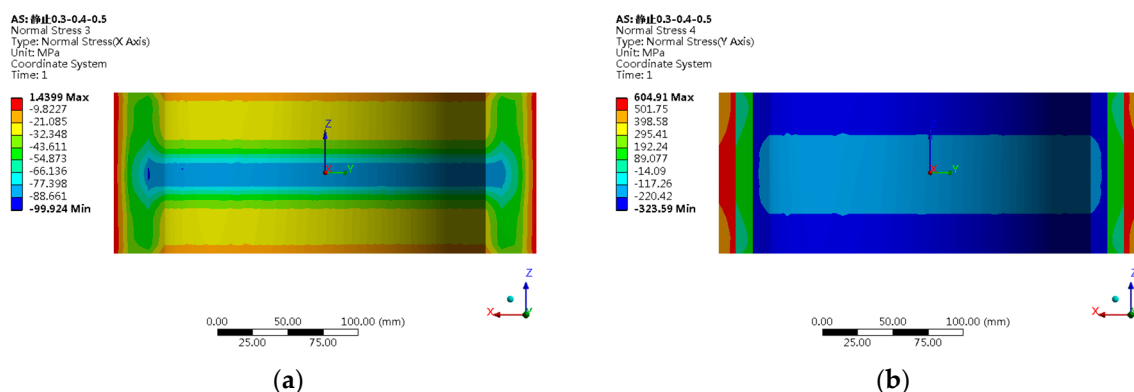(1) Stress check of flywheel rotor in a static state

Figure 11 shows the cloud diagram of an equivalent force of the flywheel rotor under a static state. The maximum equivalent stress on the flywheel rotor appears on the outer

wheel flange, and the maximum value is 630.16 Mpa, which does not exceed the strength of the wheel flange material. Because the strength of the hub material is much lower than that of the wheel flange, the maximum equivalent stress on the wheel hub appears at the junction of the spoke and the inner edge of the wheel hub. This is because when the pressure generated by the interference assembly is transferred here, the wheel hub structure becomes uneven, resulting in stress concentration at the junction. The maximum value of the equivalent stress is 432.71 Mpa. Within the yield strength of the wheel hub, the flywheel rotor does not fail in terms of the equivalent stress.

(a)

(b)
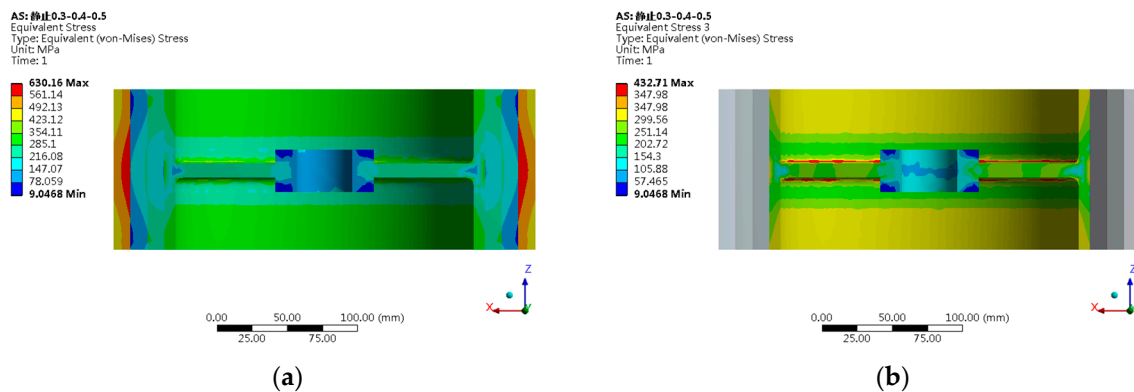
Figure 11. Equivalent stress nephogram of flywheel rotor in a static state. (**a**) Overall equivalent stress cloud diagram of flywheel rotor; (**b**) Equivalent stress cloud map of the wheel hub.

The stress nephogram of wheel flange under a static state is shown in Figure 12. The outer wheel flange's outer side bears radial tensile stress, the rest of the wheel flange bears radial compressive stress, and the flywheel is under pressure. The maximum radial compressive stress borne by the rim is located in the middle of the inner layer along the axial direction. The maximum compressive stress is 99.92 Mpa, which is less than the radial compressive strength of the wheel flange material. The maximum radial tensile stress borne by the rim is 1.44 Mpa, which is less than the radial tensile strength of the wheel flange material. The hoop stress increases from the inner layer to the outer layer and jumps at the junction of the two layers. The maximum hoop stress appears at the outer wheel flange, with a maximum value of 604.91 Mpa, less than the hoop tensile strength of the wheel flange material.

(a)

(b)

Figure 12. Wheel flange direction stress cloud in a static state. (**a**) Radial stress contour of wheel flange; (**b**) Hoop stress contour of wheel flange.
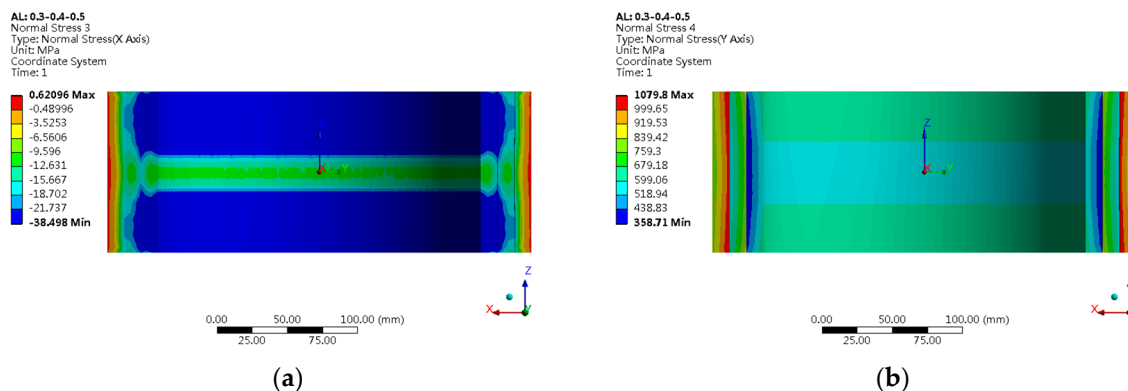
(2) Stress analysis of flywheel rotor at maximum speed

The equivalent stress nephogram of the flywheel rotor at the highest speed is shown in Figure 13. The maximum equivalent stress on the flywheel rotor appears on the inner side of the outermost rim. The maximum value is 1087.6 MPa, and the equivalent stress on the wheel flange changes in a regular layered manner, increasing in steps from the inside to the outside. The maximum equivalent stress on the wheel hub appears at the junction of the spoke and the axle hole, which is caused by the sudden change of the hub structure when the centrifugal force is transmitted from outside to inside. The maximum equivalent stress is 419.57 MPa, which is less than the yield strength of the wheel hub material. The flywheel rotor is safe at the highest speed.
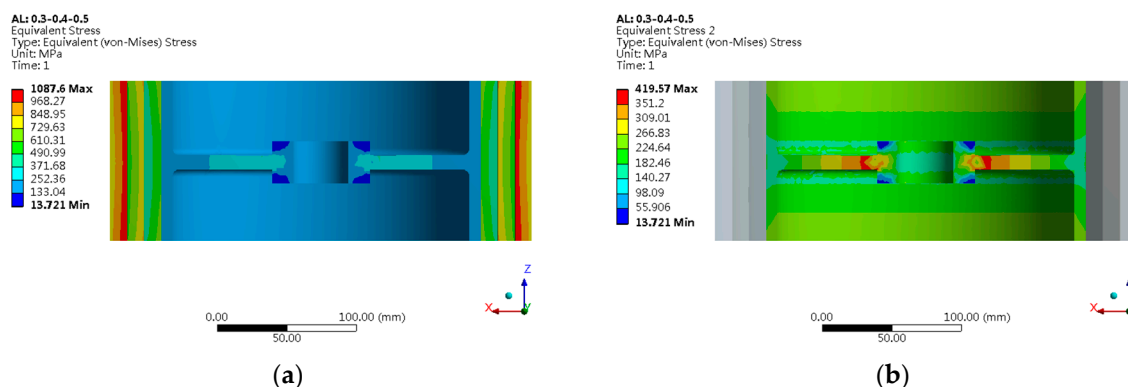
Figure 13. Equivalent stress nephogram of flywheel rotor at maximum speed. (**a**) Overall equivalent stress cloud diagram of flywheel rotor; (**b**) Equivalent stress cloud map of the wheel hub.

The radial and hoop stress contours of the flywheel rotor wheel flange at the highest speed are shown in Figure 14. Under the action of centrifugal force, the compressive stress on the wheel flange of the flywheel is greatly reduced. The maximum compressive stress on the wheel flange appears at the junction of the inner wheel flange and the wheel hub, and the maximum value is about 38.50 MPa, which is smaller than the radial compressive strength of the wheel flange material. The maximum radial tensile stress on the wheel flange appears on the outer wheel flange, and the maximum value is 0.62 MPa, less than the radial tensile strength of the wheel flange material, and no failure occurs. At the highest speed, the hoop stress decreases in steps from the inside to the outside. The maximum hoop stress on the wheel flange is 1079.8 MPa, which is much smaller than the hoop tensile strength of the wheel flange material, and no failure occurs.

Figure 14. Flywheel rotor stress nephogram at maximum speed. (**a**) Radial stress cloud diagram of flywheel rotor; (**b**) Hoop stress cloud diagram of flywheel rotor.

The outer layer and the middle layer of the flywheel rotor are most easily separated. In order to further confirm the safety of the flywheel rotor, extract the cloud diagram of

the contact state between the outer layer and the middle layer of the flywheel rotor wheel flange, as shown in Figure 15a. It can be seen that the outer layer and the middle layer of the wheel flange are in good contact without separation. As shown in Figure 15b, the contact pressure nephogram between the outer and middle layers of the wheel flange is extracted. It can be seen that the pressure between the wheel flange and the wheel hub is lower in the middle and higher on both sides along the axial direction. That is, the middle direction is the most prone to loosening, and the minimum pressure is 13.74 Mpa, which indicates that there is always pressure between the wheel flange layers at the highest speed, and the flywheel rotor is safe.

(a) (b)
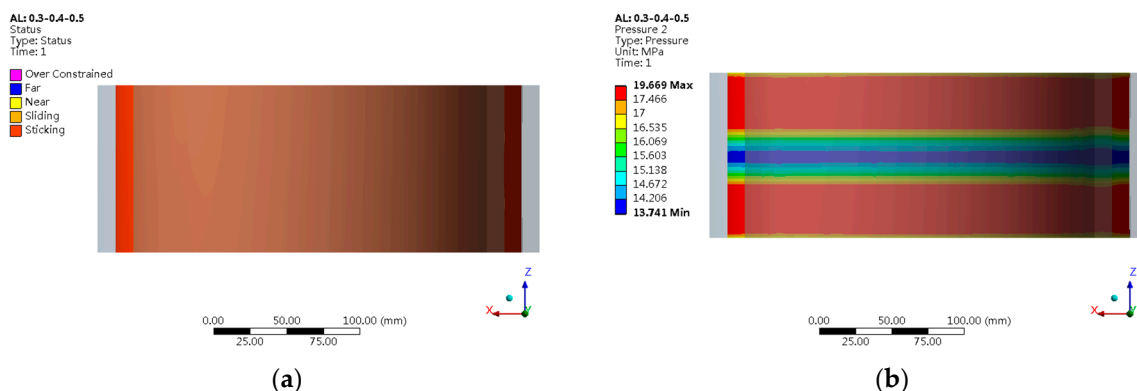
Figure 15. Contact cloud diagram of flywheel rotor. (**a**) Contact state cloud map; (**b**) Contact pressure cloud map.

5. Conclusions

In this paper, the design and analysis of the flywheel system used in an electric vehicle are taken as the research object. Based on the vehicle dynamics characteristics, the energy storage and power requirements of the whole vehicle for the flywheel are analyzed and determined. The mathematical model of the flywheel rotor stress in a multi-layer interference assembly is established. The size design of the flywheel battery rotor is completed, and the stress analysis of the flywheel rotor with multi-layer flange interference assembly is carried out. Based on the finite element software Ansys, the influence of the number of layers of the flywheel rotor wheel flange and the amount of interference between layers on the flywheel rotor stress distribution are analyzed emphatically and the reasonable flange structure is selected. The stress check is carried out under two extreme conditions to ensure its strength meets the use requirements. The research conclusions are as follows:

(1) The selection of the power threshold should try to make the power cover most of the required power of the whole vehicle. If the power threshold is too small, the workload of the flywheel battery will be too heavy. If the threshold value is too high, the flywheel battery will not be able to "cut peaks and make up valleys" for the output power of the lithium battery.

(2) The radial compressive stress can be generated in the flywheel rotor by using the interference assembly method to improve the radial strength of the flywheel rotor. Still, the increase of the radial strength will sacrifice some of the circumferential strength. Multi-layer interference assembly can improve the flywheel rotor's stress level, improve the flywheel rotor's strength, and reduce the machining difficulty of the flywheel rotor. However, the wheel flange cannot be infinitely layered. When there are too many layers, material failure occurs due to excessive radial compressive stress. The three layers interference assembly with a layer thickness of 12 mm is adopted, which can meet the assembly stress requirements of a super highspeed flywheel rotor.

(3) The hoop stress will jump at the junction of the two layers, and the jump amplitude is proportional to the interference at the junction. The interference between the outer layer and the middle layer will have a great impact on the peak hoop stress. Therefore,

it is necessary to decrease the interference at the junction to avoid fatigue failure caused by the long-term stress of the wheel hub.

(4) From the point of view of improving the stress level of the flywheel rotor, when selecting the interference between wheel flange layers of the flywheel rotor, the smaller interference should be selected in the inner layer of the wheel flange, and the larger interference should be selected in the outer layer. The interference between inner layer and wheel hub, middle layer and inner layer, and outer layer and middle layer are designed to be 0.3, 0.4 and 0.5 mm, respectively, which can meet the design requirements.

Author Contributions: Conceptualization, P.W.; Data curation, T.G. and R.L.; Formal analysis, B.S.; Funding acquisition, B.S. and T.Z.; Investigation, P.W., T.G., R.L. and J.Y.; Methodology, P.W.; Project administration, B.S.; Resources, P.W. and B.S.; Software, R.L.; Supervision, B.S. and T.Z.; Validation, T.G.; Visualization, R.L. and J.Y.; Writing—original draft, P.W.; Writing—review & editing, T.G. All authors have read and agreed to the published version of the manuscript.

Data Availability Statement: Not applicable.

Conflicts of Interest: The authors declare no conflict of interest.

References

1. Hedlund, M.; Lundin, J.; De Santiago, J.; Abrahamsson, J.; Bernhoff, H. Flywheel energy storage for automotive applications. *Energies* **2015**, *8*, 10636–10663. [CrossRef]
2. Yongjie, H.A.; Chong, L.I.; Haoyu, W.A.; Zhengyi, R.E. Analysis of the stresses and displacements for a composites interference fit multi-rim flywheel. *Energy Storage Sci. Technol.* **2018**, *7*, 815–820.
3. Xingjian, D.A.; Kunpeng, W.E.; Xiaozhang, Z.H.; Xinjian, J.I.; Kai, Z.H. A review on flywheel energy storage technology in fifty years. *Energy Storage Sci. Technol.* **2018**, *7*, 765–782.
4. Rupp, A.; Baier, H.; Mertiny, P.; Secanell, M. Analysis of a flywheel energy storage system for light rail transit. *Energy* **2016**, *107*, 625–638. [CrossRef]
5. Wang, Q.; Mah, J.S. The Role of the Government in Development of the Electric Vehicle Industry of China. *China Rep.* **2022**, *58*, 194–210. [CrossRef]
6. Ma, S.C.; Xu, J.H.; Fan, Y. Characteristics and key trends of global electric vehicle technology development: A multi-method patent analysis. *J. Clean. Prod.* **2022**, *338*, 130502. [CrossRef]
7. Sun, B.B.; Gu, T.Q.; Wang, P.W.; Zhang, T.Z.; Wei, S.B. Optimization Design of Powertrain Parameters for Electromechanical Flywheel Hybrid Electric Vehicle. *IAENG Int. J. Appl. Math.* **2022**, *52*, 450–457.
8. Wu, J.; Zhang, J.; Tian, Y.; Li, L. A Novel Adaptive Steering Torque Control Approach for Human–Machine Cooperation Autonomous Vehicles. *IEEE Trans. Transp. Electrif.* **2022**, *7*, 2516–2529. [CrossRef]
9. Kachhwaha, A.; Rashed, G.I.; Garg, A.R.; Mahela, O.P.; Khan, B.; Shafik, M.B.; Hussien, M.G. Design and Performance Analysis of Hybrid Battery and Ultracapacitor Energy Storage System for Electrical Vehicle Active Power Management. *Sustainability* **2022**, *14*, 776. [CrossRef]
10. Ehsani, M.; Gao, Y.; Emadi, A. *Modern Electric, Hybrid Electric, and Fuel Cell Vehicles: Fundamentals, Theory, and Design*; CRC Press: Boca Raton, FL, USA, 2017.
11. Itani, K.; De Bernardinis, A.; Khatir, Z.; Jammal, A. Comparative analysis of two hybrid energy storage systems used in a two front wheel driven electric vehicle during extreme start-up and regenerative braking operations. *Energy Convers. Manag.* **2017**, *144*, 69–87. [CrossRef]
12. Huang, C.N.; Chen, Y.S. Design of magnetic flywheel control for performance improvement of fuel cells used in vehicles. *Energy* **2017**, *118*, 840–852. [CrossRef]
13. Hansen, J.G.R.; O'Kain, D.U. *An Assessment of Flywheel High Power Energy Storage Technology for Hybrid Vehicles*; Oak Ridge National Laboratory: Oak Ridge, TN, USA, 2011.
14. Arani, A.K.; Karami, H.; Gharehpetian, G.B.; Hejazi, M.S. Review of flywheel energy storage systems structures and applications in power systems and microgrids. *Renew. Sustain. Energy Rev.* **2017**, *69*, 9–18. [CrossRef]
15. Sun, B.B.; Gao, S.; Ma, C. System Power Loss Optimization of Electric Vehicle Driven by Front and Rear Induction Motors. *Int. J. Automot. Technol.* **2018**, *19*, 121–134. [CrossRef]

16.   Tutuncu, N. Effect of anisotropy on stresses in rotating discs. *Int. J. Mech. Sci.* **1995**, *37*, 873–881. [CrossRef]
17.   Wang, X.C. *Design of Carbon Fiber Composite Flywheel*; Wuhan University of Technology: Wuhan, China, 2013.